Prabha Materials Science Letters
Vol. 5, No. 2, 362-377, 2026
https://doi.org/10.33889/PMSL.2026.5.2.020

Study of Photocatalytic Activity of $Mn_{1-x}Cu_xS$ Nanoparticles

Purnima Gasso
Department of Physics,
Punjabi University, 147002, Patiala, Punjab, India.
E-mail: purnima_rs23@pbi.ac.in

Ashok Kumar Malik
Department of Chemistry,
Punjabi University, 147002, Patiala, Punjab, India.
E-mail: malik_chem2002@yahoo.co.uk

Karamjit Singh
Department of Physics,
Punjabi University, 147002, Patiala, Punjab, India.
Corresponding author: dhaliwalkaramjit@gmail.com, dhaliwalkaramjit@pbi.ac.in

(Received on November 30, 2025; Revised on February 3, 2026 & May 3, 2026 & May 27, 2026;
Accepted on May 30, 2026)

Abstract
Manganese Sulfide (MnS) is a wide band gap (3.7 eV) p-type semiconductor comprising three crystalline (cubic rock-salt MnS, cubic zincblende MnS, and hexagonal wurtzite MnS structures) polymorphs. Pristine and copper-doped MnS nanoparticles have been synthesized using a facile chemical co-precipitation method. Crystallographic, morphological, qualitative, and quantitative characteristics of synthesized $Mn_{1-x}Cu_xS$ ($0 \leq x \leq 0.09$) nanoparticles have been studied using X-Ray Diffraction (XRD), Field-Emission Scanning Electron Microscope (FE-SEM), Energy Dispersive X-ray Spectroscopy (EDS), Fourier Transform Infrared Spectroscopy (FTIR), and UV-Visible absorption spectroscopy. Recorded diffractograms reveal the formation of a dual crystal phase of MnS as hexagonal wurtzite gamma MnS and cubic rock-salt alpha MnS phase, while FE-SEM analyses indicate the cauliflower morphology of synthesized nanoparticles. The direct band gap energy for Mn_1Cu_0S NPs and $Mn_{0.91}Cu_{0.09}S$ NPs was calculated to be 3.85 eV and 3.80 eV, respectively. Photocatalytic activity of synthesized nanoparticles has been studied using Rhodamine B (RhB) dye as a test contaminant in aqueous media under UV (UVC; 2×30 W) irradiation. $Mn_{0.93}Cu_{0.07}S$ NPs exhibited the highest photocatalytic activity with a degradation efficiency of 46.72%. Photocatalytic activity dependence on doping concentration and morphology has been thoroughly studied to explore the potential of synthesized nanoparticles for polluted water purification.

Keywords- Manganese sulfide, Nanoparticles, Photocatalysis, Crystallography, Morphology.

1. Introduction

Increasing globalization and industrialization are causing extreme exploitation to the quality of water day by day. Water is one of the main sources for the existence of life on earth, and only 0.5% of the 3% fresh water is available for human utilization. Water contamination caused due to the use of dyes from small to large-scale industries encompassing tanneries, cosmetics, textile, food, and medical sectors has been causing serious issues. Being highly carcinogenic and non-biodegradable, contamination of water due to dyes causes severe implications to aquatic life as well as human life, imparting life-threatening diseases like cancer (Barry & Chorley, 2009; Muthu et al., 2021; Woetzel et al., 2020). Synthetic dyes such as Rhodamine B (RhB), Methylene Blue (MB), Methyl Orange (MO), Congo Red (CR), and Methyl Violet (MV) are one of the most common types of water contaminants, regarded as a serious threat to the environment and humans (Salem et al., 2022; Shanker et al., 2017; Somnath et al., 2022).

To deal with the increasing environmental crisis, one requires the efficient utilization of green energy and green chemistry. Development of advanced oxidation processes (AOPs) emerges as an effective method for the treatment of contaminated water in comparison to traditional methods. Photocatalysis has attracted a lot of attention for its ability to utilize green solar energy and advanced oxidation processes for the degradation of pollutants (Chen et al., 2010; Chen et al., 2020; Pawar & Lee, 2015). Semiconductor nanomaterials have been an area of research since the seventies and early eighties, due to their ability to split water and their capability of removing pollutants (organic and inorganic) for the purification of water (Mills et al., 1993; Mills & Le Hunte, 1997). Successful decomposition of water was demonstrated for the first time by Fujishima and Honda using a TiO_2 semiconductor photoanode coupled with a Pt cathode (Fujishima & Honda, 1972).

Relative to the others, semiconductor metal chalcogenides have been a focus of interest in recent years due to their unique properties, low band gap energy, and ability to synthesize in ambient conditions. Transition metal sulfides, such as vanadium sulfide, copper sulfide, cobalt sulfide, iron sulfide, nickel sulfide, and manganese sulfide compounds, have been widely explored for water-splitting-catalytic applications (Guo et al., 2020; Qurashi, 2014; Wang et al., 2023). Manganese sulfide (MnS), comprising a wide band gap of 3.7 eV (Huffman & Wild, 1967; Lu et al., 2001; Wang et al., 1996) offer remarkable advantages owing to its diverse crystal structure, mechanical strength, thermal stability, high electrical conductivity, high electrochemical, optical, and catalytic properties. Its unique properties make it suitable for diverse applications such as in solar cells, supercapacitors, thermoelectric devices, photonics, photocatalysis, and lithium-ion/sodium-ion batteries (LIBs/SIBs) (Hao et al., 2017; Jamal et al., 2023; Lee et al., 2020; Liu et al., 2018; Swathi et al., 2021; Yang et al., 2012). MnS comprises three crystalline polymorphs: α-MnS, β-MnS, and γ-MnS. α-MnS or rock-salt structure has cubic phase ($a = b = c = 5.224$ A°, space group Fm3m). β-MnS has a cubic zinc-blende crystal structure ($a = b = c = 5.615$ A°, space group $F\bar{4}3m$), while hexagonal γ-MnS has a wurtzite crystal structure ($a = b = 3.979$ A° and $c = 6.446$ A°, space group $P6_3mc$). β-MnS and γ-MnS are metastable in nature, which can be transformed into more stable α-MnS at high temperature (100-400°C) or high pressure (Michel et al., 2006; Puglisi et al., 2010; Rao & Pisharody, 1976; Rui et al., 2014).

Various morphologies of MnS, such as nanowires (Brieler et al., 2004; Kim et al., 2006), nano octahedrals (Gui et al., 2011; Puglisi et al., 2010), nanobelts (Ma et al., 2008), nanotubes (Liu et al., 2018), quantum dots (Agoro & Meyer, 2022), and thin films (Fan et al., 2003; Ibrahim, 2021; Yıldırım et al., 2016) has been synthesized using a variety of synthesis processes. Lu et al. in 2001 synthesized metastable (β and γ) and stable (α) MnS crystallites via the solvothermal method. Various solvents (such as benzene, tetrahydrofuran (THF), and water) have been used to synthesize polymorphs at 190-200°C (Lu et al., 2001). In 2021, Swathi et al. synthesized MnS nanostructures using a hydrothermal technique with varying concentrations of hydrazine hydrate to study the electrochemical water oxidation and photocatalytic hydrogen production. X-ray diffraction (XRD) analysis confirmed the formation of α-MnS nanostructures (Swathi et al., 2021). Successive Ionic Layer Adsorption and Reaction (SILAR) method (Yıldırım et al., 2016), spray pyrolysis technique (Ibrahim, 2021), refluxing method (Lee et al., 2020), one-pot solvent thermal approach (Yang et al., 2012), molten salt solid state reaction method (Heiba et al., 2022), and the wet chemical technique (Veeramanikandasamy et al., 2016) have also been used for the synthesis of MnS.

In the present research work, pristine and copper-doped MnS nanoparticles (NPs) have been synthesized using a non-toxic, cost-effective, and less time-consuming facile chemical co-precipitation method. Doping of copper (Cu) has been performed to ameliorate the photocatalytic activity of MnS. To the best of our knowledge, the photocatalytic activity of Cu-doped MnS nanoparticles for the degradation of RhB dye specifically has not been reported to date. This is the first study to investigate the advanced wastewater

treatment application of $Mn_{1-x}Cu_xS$ ($0 \leq x \leq 0.09$) nanoparticles synthesized via a facile co-precipitation method for the degradation of RhB dye.

2. Materials and Methods

2.1 Synthesis

All the analytical grade chemicals and organic solvents were used without any further purification. The $Mn_{1-x}Cu_xS$ ($0 \leq x \leq 0.09$) NPs were synthesized in the ambient air using a facile chemical co-precipitation method (Viswanath et al., 2014). 0.5 M solutions of manganese and sulphur precursors were prepared separately by dissolving 6.1272 g of manganese acetate tetrahydrate [$(CH_3COO)_2Mn.4H_2O$], and 1.9512 g of sodium sulfide (Na_2S) in 50 ml (water:ethanol = 1:1) solvent. Variable concentrations of copper acetate monohydrate [$Cu(CO_2CH_3)_2.H_2O$] solution as copper precursor were added to the prepared manganese precursor solution under vigorous stirring, followed by dropwise addition of a 50 ml solution of sulfur precursor at 70 °C (±5°C). The obtained product was filtered and washed thoroughly with de-ionized water and ethanol several times. The final product was dried in a vacuum oven at 150 °C for 3 hr.

2.2 Characterization

Crystallographic characterization of synthesized $Mn_{1-x}Cu_xS$ ($0 \leq x \leq 0.09$) nanoparticles has been performed using X-Ray Diffractometer (XRD, Smartlab Rigaku) with monochromatic Cu K_α radiation (λ =0.154 nm) by keeping step size 0.02° in the 2θ range of 25° to 75°. Morphological characterization of synthesized materials has been done using a Field-Emission Scanning Electron Microscope (FE-SEM; Hitachi SU 8010 Series) at an accelerating voltage of 10.0 kV and working distance (WD) of 7.8 mm. Prepared samples were fixed onto a metal stub using conductive double-adhesive carbon tape, followed by gold coating to prevent charge buildup during FE-SEM analyses. The qualitative and quantitative analysis is conducted using Energy Dispersive X-Ray Spectroscopy (EDS) to study the elemental composition of the synthesized nanoparticles, and a Fourier Transform Infrared spectrometer (FTIR; Shimadzu IRSpirit-X Series) to determine the functional groups of the synthesized nanoparticles. Optical properties were studied using UV-Visible absorption spectroscopy (Hitachi U-2900 spectrophotometer).

2.3 Photocatalytic Activity

The photocatalytic activity of synthesized $Mn_{1-x}Cu_xS$ ($0 \leq x \leq 0.09$) NPs has been studied for the degradation of RhB dye at room temperature. The experiment was performed in an indigenous UV reactor under the UV (2×30 W) irradiation in the wavelength range 200-280 nm. 40 mg of the photocatalyst was dispersed into 200 ml deionized solution of 10^{-5} M RhB dye. In order to attain adsorption-desorption equilibrium in the photocatalytic solution, the reaction mixture was magnetically stirred in the dark for 1 hour. Then the suspension solution was irradiated with UV radiation, and absorption spectra of the sample were measured for 180 minutes with sampling at every 30 min time interval. The collected samples were centrifuged and analyzed with a UV-Visible absorption spectrophotometer (Hitachi U-2900). The photocatalytic degradation efficiency of RhB was examined at a characteristic wavelength of 553.5 nm. The photocatalytic degradation efficiency (PD) of the dye was calculated using the following Equation (1):

$$PD = \frac{(A_0 - A_t)}{A_0} \times 100 \quad (1)$$

where, A_0 is the absorbance of the dye solution before the photo degradation, and A_t is the absorbance of remnant dye after photo degradation for a certain time 't'.

3. Results and Discussions

3.1 Crystallographic Characterization

The recorded XRD patterns of $Mn_{1-x}Cu_xS$ ($0 \leq x \leq 0.09$) nanoparticle series are shown in **Figure 1**. Diffraction peaks confirmed the presence of dual γ-MnS phase (JCPDS File No.: 00-040-1289) and α-MnS phase (JCPDS File No.: 96-900-5944). XRD peaks at 26.00°, 27.66°, 38.28°, 45.72°, 49.94°, 54.44°, and 55.48° corresponding to crystallographic planes (100), (002), (102), (110), (103), (112), and (201) belongs to the hexagonal γ-MnS phase, whereas peaks at 31.14°, and 36.08° corresponding to crystallographic planes (111), and (020) belongs to the cubic α-MnS phase respectively. An additional Mn_3O_4 (JCPDS File No.: 01-080-0382) phase is also observed at 2θ values of 28.92°, 32.46°, 36.56°, 44.38°, 51.04°, 58.48°, 59.92°, and 64.56° corresponding to (112), (103), (202), (220), (105), (321), (224), and (400) respectively. The presence of Mn_3O_4 phase can be attributed to the pronounced susceptibility of MnS to oxidation during both the pre-synthesis and post-synthesis processes (Admuthe et al., 2020; Heiba et al., 2022). A slight shift of the (020) diffraction peak towards a higher diffraction angle as shown in **Figure 2**, reveals the compressive strain developed in the host lattice due to doping. Average crystallite size has been determined using the Scherrer equation (Holzwarth & Gibson, 2011).

$$D = \frac{K\lambda}{\beta \cos\theta} \tag{2}$$

where, K is the Scherrer constant (0.89), λ is the wavelength, β is the full-width at half maximum, and θ is the Bragg's angle.

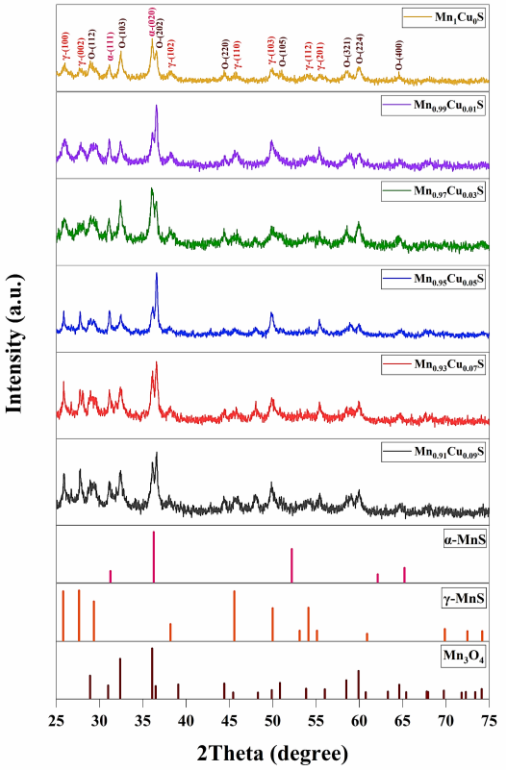

Figure 1. X-Ray diffractograms of $Mn_{1-x}Cu_xS$ ($0 \leq x \leq 0.09$) nanoparticles. The JCPDS File No.: 00-040-1289 for γ-MnS phase, JCPDS File No.: 96-900-5944 for α-MnS phase, and JCPDS File No.: 01-080-0382 for Mn_3O_4 phase are shown as references. The Miller indices are shown in the inset of Mn_1Cu_0S, where α, γ, and O represent α-MnS phase, γ-MnS phase, and Mn_3O_4 phase, respectively.

The average crystallite size values calculated for Mn_1Cu_0S, $Mn_{0.99}Cu_{0.01}S$, $Mn_{0.97}Cu_{0.03}S$, $Mn_{0.95}Cu_{0.05}S$, $Mn_{0.93}Cu_{0.07}S$, and $Mn_{0.91}Cu_{0.09}S$ nanoparticles are 17.48 nm, 23.05 nm, 15.74 nm, 18.30 nm, 19.34 nm, and 17.38 nm, respectively. The ionic radius of the host Mn^{2+} ion (~ 0.80 A°) is larger than the dopant Cu^{2+} ion (~0.73 A°). The difference in ionic radii results in the creation of compressive strain and lattice distortion within the host material. The decrease in crystallite size can be attributed to the introduction of stress and resulting crystal imperfection on the doping of copper, which prohibits the growth (Heiba et al., 2022; Veeramanikandasamy et al., 2016).

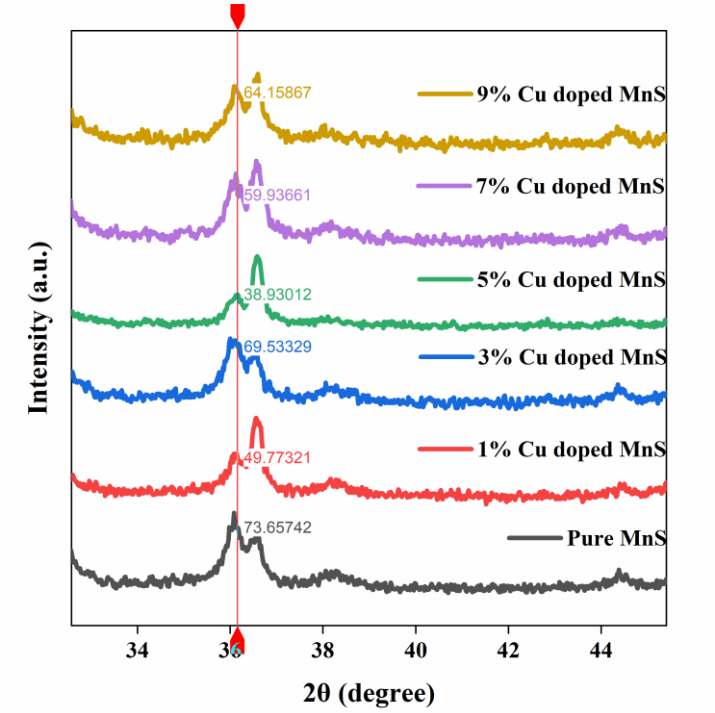

Figure 2. Comparison of the diffraction peak intensity and peak shifting corresponding to the (020) plane of the cubic α-MnS phase.

3.2 Morphological Analysis

FE-SEM micrographs of pristine MnS and copper-doped MnS are shown in **Figure 3**. The recorded micrographs of the synthesized nanoparticles have revealed a cauliflower shape. It can be seen from the micrographs that particle size distribution is heterogeneous in nature. For the precise quantitative analysis of FESEM micrographs, ImageJ software has been used to plot a histogram with a distribution curve, where the x-axis denotes the particle size, and the y-axis represents the particle counts (**Figure 4**). Average particle size calculated from raw data was determined to be 25 ± 8 nm, and 21 ± 5 nm for Mn_1Cu_0S NPs and $Mn_{0.91}Cu_{0.09}S$ NPs, respectively. Decrease in particle size justifies the incorporation of copper ions in the pure MnS lattice structure, which is in agreement with XRD results.

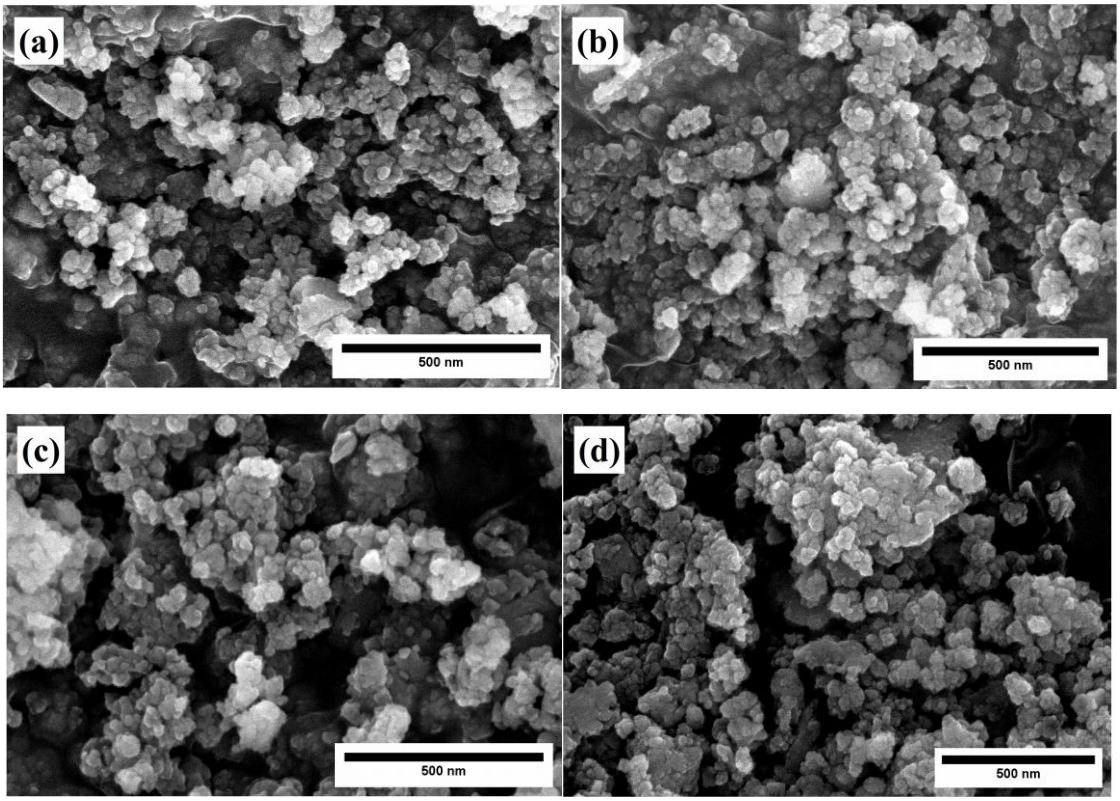

Figure 3. FE-SEM micrographs: (a) & (b) Mn_1Cu_0S NPs; (c) & (d) $Mn_{0.91}Cu_{0.09}S$ NPs.

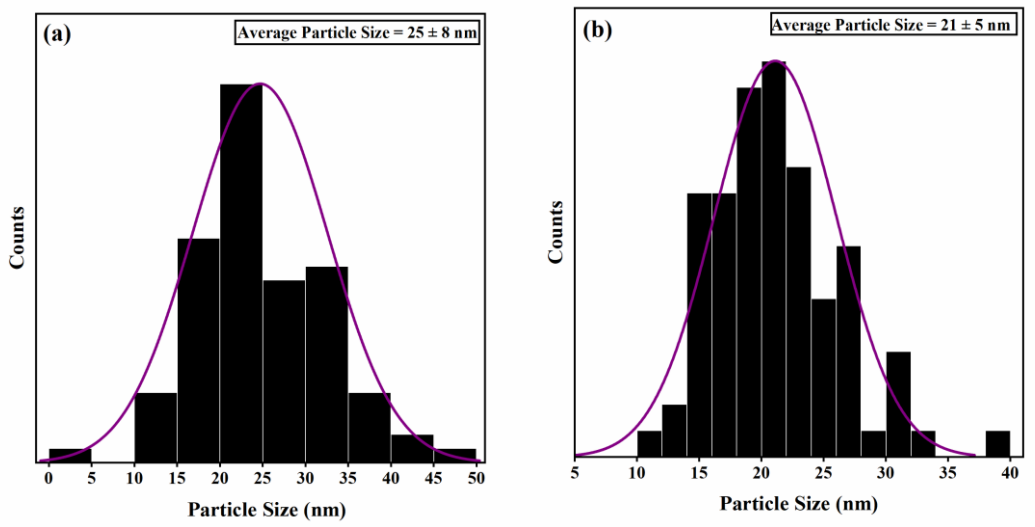

Figure 4. Particle size distribution curve: (a) Mn_1Cu_0S NPs; (b) $Mn_{0.91}Cu_{0.09}S$ NPs.

3.3 Energy Dispersive X-Ray Spectroscopy (EDS)

Energy dispersive X-Ray spectroscopy was used to determine the elemental composition of the synthesized nanoparticles. **Figure 5(a)** shows the EDS spectra of Mn_1Cu_0S NPs, which reveal the presence of manganese (Mn), sulfur (S), oxygen (O), and carbon (C) elements with atomic percentages of 42.17 %, 10.62 %, 37.76 %, and 9.44%, respectively. The presence of oxygen confirmed the formation of the Mn_3O_4 phase, whereas the carbon tape used during sample preparation resulted in a carbon peak. Along with Mn and S, the presence of copper was confirmed in the case of $Mn_{0.91}Cu_{0.09}S$ nanoparticles with atomic percentages of 66.68 %, 24.08 %, and 9.24 %, respectively, as shown in **Figure 5(b)**. The peaks observed in the EDS spectra are in agreement with the expected photon energies (in eV) of the principal K-, L-, and M- shell emission lines (Thompson & Vaughan, 2001).

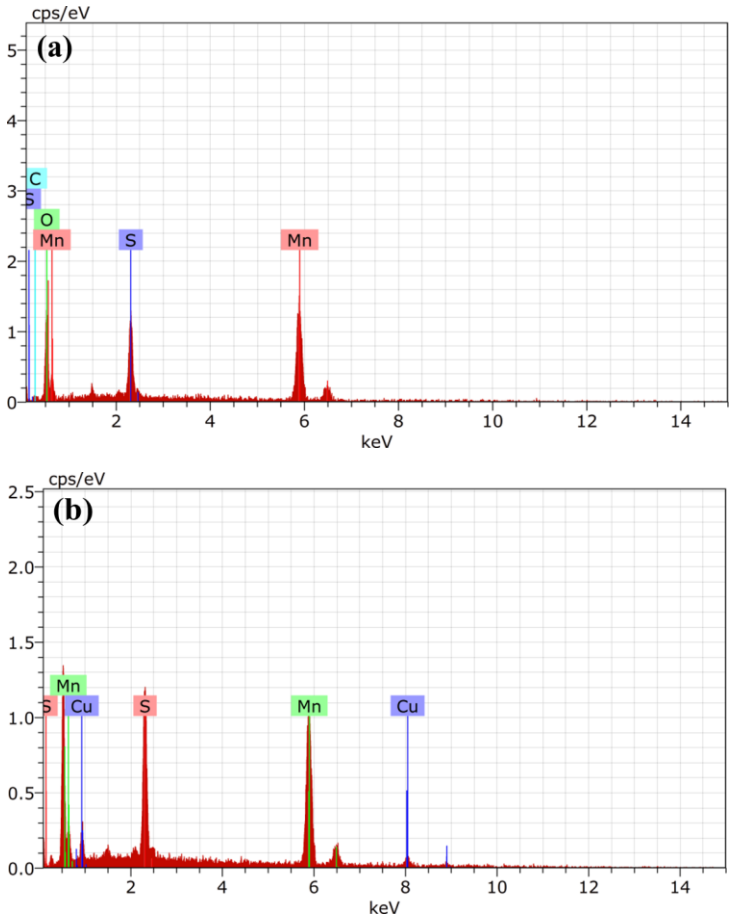

Figure 5. EDS spectra: (a) Mn_1Cu_0S NPs; (b) $Mn_{0.91}Cu_{0.09}S$ NPs.

3.4 Fourier Transform Infrared Spectrometer (FTIR)

Study of FTIR spectra provides information about the chemical components present in the synthesized nanoparticles. **Figure 6** shows the FTIR spectra of Mn_1Cu_0S NPs and $Mn_{0.91}Cu_{0.09}S$ NPs. The vibrational bands observed at 480.64 cm^{-1} and 602.59 cm^{-1} are attributed to Mn-S stretching vibrational modes, and interaction between the vibrational mode of sulfide ions (S-S bond), respectively. The characteristic peaks at 1147.80 cm^{-1}, 2361.60 cm^{-1} and 2979.98 cm^{-1} correspond to the stretching modes of the C=O bond, C-H

bond, and C-O bond, respectively (Chen et al., 2016; Heiba et al., 2015; Lalithambika et al., 2019; Liu et al., 2014). Copper doping resulted in a red shift of the vibrational bands, which can be credited to the heavier mass of Cu in comparison to Mn and the introduction of compressive strain, weakening the bond strength within the crystal lattice (Heiba et al., 2022).

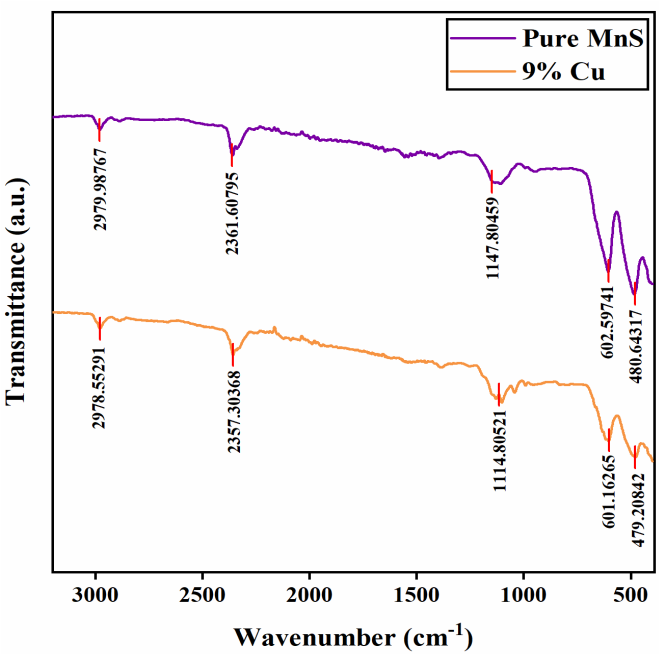

Figure 6. FTIR spectra of Mn_1Cu_0S NPs and $Mn_{0.91}Cu_{0.09}S$ NPs.

3.5 Study of Optical Properties

The optical behaviour of synthesized nanostructures was studied using UV-Visible absorption spectrophotometer (λ ~ 220 to 800 nm). **Figures 7** and **8** show the absorbance spectra for both Mn_1Cu_0S NPs and $Mn_{0.91}Cu_{0.09}S$ NPs, along with the Tauc plots (inset) to determine the band gap energy, respectively (Makuła et al., 2018). Recorded spectra reveal that synthesized materials have a broad absorption profile in the UV range. A red shift in the absorbance spectra of $Mn_{0.91}Cu_{0.09}S$ NPs in comparison Mn_1Cu_0S NPs has been observed, as evidenced by the calculated band gap values. This can be attributed to the lattice strain created due to copper doping. The band gap has been calculated using the Tauc's relation as given in Equation (3),

$$(\alpha h\nu)^n = A(h\nu - E_g) \quad (3)$$

Here, α is the absorption coefficient, hν is the photon energy, A is a proportionality constant, and the exponent n depends on the type of electronic transition in the material. For direct band gaps, n = 2, and for indirect band gaps, n = 1/2. The plot between $(\alpha h\nu)^2$ vs. energy (eV) measures the direct band gap energy for Mn_1Cu_0S NPs and $Mn_{0.91}Cu_{0.09}S$ NPs to be 3.85 eV and 3.80 eV, respectively, which is in good agreement with previously reported studies (Kayestha & Hajela, 1995; Veeramanikandasamy et al., 2016).

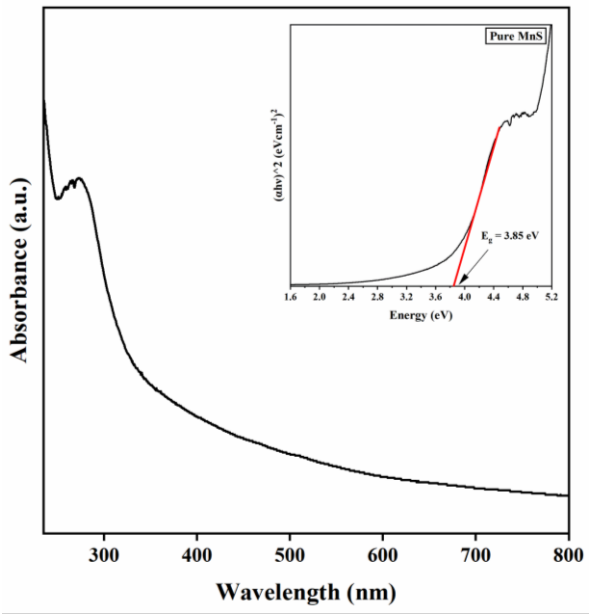

Figure 7. UV-Visible absorption spectra of Mn_1Cu_0S NPs; (Inset) Tauc's plot of Mn_1Cu_0S NPs.

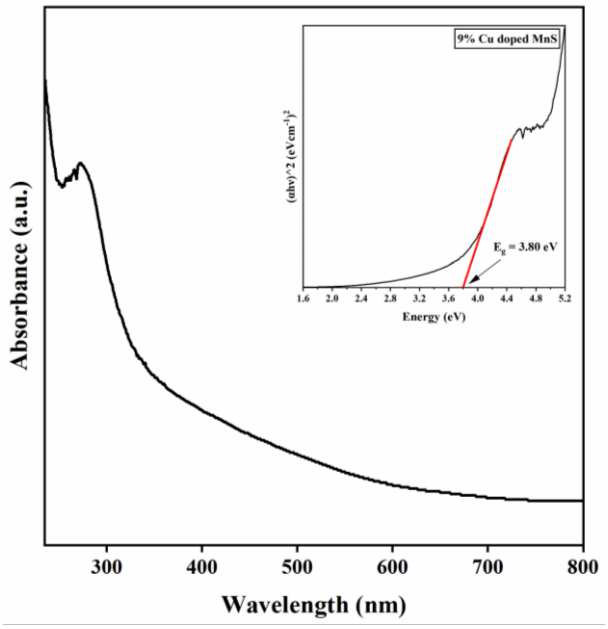

Figure 8. UV-Visible absorption spectra of $Mn_{0.91}Cu_{0.09}S$ NPs; (Inset) Tauc's plot of $Mn_{0.91}Cu_{0.09}S$ NPs.

3.6 Photocatalytic Degradation of RhB Dye

The photocatalytic activity of $Mn_{1-x}Cu_xS$ ($0 \leq x \leq 0.09$) NPs has been studied in detail using UV-Visible absorption spectroscopy. The photocatalytic degradation efficiency of RhB dye was examined at λ_{max} = 553.5 nm. The pristine and copper-doped MnS nanoparticles served as good photocatalysts in the effective

degradation of RhB dye, as shown in **Figure 9**. UV radiation exposure results in the formation of photon-excited charge carriers in NPs, which may recombine (radiatively or non-radiatively) or participate in oxidation and reduction reactions on the surface of the photocatalyst, leading to the degradation of pollutants. The probability of charge carriers participating in the redox reactions increases with a delay in the recombination rate, which can be achieved by the introduction of defect states via doping. Copper, a transition metal ion, which has low formation energy and high ionization energy, can easily incorporate into the MnS lattice. Defect states created with the doping of copper in the MnS cause a delay in recombination time i.e., enhancement in the excited state lifetime is observed. Thus, copper doping is conducted to lengthen the recombination time of charge carriers, which increases the charge carrier excited state lifetime, allowing them to carry out the redox reaction, resulting an increase in the photocatalytic activity (Heiba et al., 2022; Uma et al., 2023; Veeramanikandasamy et al., 2016). Dye adsorption percentage on the surface of the synthesized $Mn_{1-x}Cu_xS$ ($0 \leq x \leq 0.09$) NPs has been presented in **Figure 10** after achieving adsorption-desorption equilibrium in the photocatalytic solution under dark conditions for 1 hour. The plot reveals noticeable variation in the adsorption percentage among the doped samples, indicating the changes in surface properties and active adsorption sites due to doping.

Photocatalytic degradation efficiency of the synthesized nanoparticles has been observed to be 37.91%, 27.07%, 32.23%, 44.36%, 46.72%, and 37.91% for Mn_1Cu_0S, $Mn_{0.99}Cu_{0.01}S$, $Mn_{0.97}Cu_{0.03}S$, $Mn_{0.95}Cu_{0.05}S$, $Mn_{0.93}Cu_{0.07}S$, and $Mn_{0.91}Cu_{0.09}S$ NPs, respectively, as shown in **Figure 11**. $Mn_{0.99}Cu_{0.01}S$ and $Mn_{0.97}Cu_{0.03}S$ NPs exhibit low photocatalytic degradation efficiency compared to Mn_1Cu_0S NPs. At low concentration, substitution of the host ions with copper ions results in the introduction of discrete deep trapping states in the forbidden energy gap of the host material, accelerating the photogenerated charge carriers' recombination rate and hence restricting their participation in the generation of reactive oxygen species (ROS). The low photocatalytic activity can also be justified by the reduced surface adsorption trend as observed in **Figure 10**. Since photocatalytic redox reactions occur on the catalyst surface, reduced adsorption limits the surface activity, suppressing the interfacial oxidation reactions and hence decreasing the overall efficiency of $Mn_{0.99}Cu_{0.01}S$ and $Mn_{0.97}Cu_{0.03}S$ NPs. Photocatalytic degradation efficiency was observed to be maximum for $Mn_{0.93}Cu_{0.07}S$ NPs, justifying the optimum doping concentration. The increase in photocatalytic efficiency can be attributed to the reduction of the effective band gap on doping, resulting in charge separation, which effectively suppresses the electron-hole pair recombination and promotes the participation of charge carriers in the redox reaction. Additionally, the presence of mixed oxide phases facilitates the catalytic behaviour by providing complementary band-edge positions and redox potential. The formation of this heterostructure promotes efficient separation of photogenerated electron–hole pairs, thereby enhancing reaction kinetics and overall photocatalytic activity (Ali et al., 2024; Heiba et al., 2022; Janani et al., 2020; Liu et al., 2020). Further increase in doping concentration beyond the optimum threshold resulted in a decrease in the degradation efficiency of $Mn_{0.91}Cu_{0.09}S$ NPs due to the screening effect that occurs, blocking the photon absorption on active surface sites of the photocatalyst. Further, high copper concentration introduces defect states that act as recombination centers, thus decreasing its overall photocatalytic degradation efficiency.

The mixed behaviour of the photocatalytic activity can be attributed to the synergistic effect of the dual phase along oxide phase in the synthesized nanoparticles, which causes the change in electronic band structure and formation of a heterogeneous interface, influencing the recombination rate and migration pathways of the photoexcited charge carriers. Alpha MnS provides good thermodynamic stability but exhibits low photocatalytic activity. Whereas, gamma MnS is a metastable phase and generally demonstrates higher photocatalytic activity. The synergy of both phases provides efficient water stability and superior photocatalytic activity, thereby displaying their potential for efficient wastewater remediation. Due to its smaller band gap, MnS provides catalytic degradation only in the visible region. Mn_3O_4 acts as

a co-catalyst, extending the absorption range of the material and increasing its stability. The interface between MnS and Mn_3O_4 acts as a charge transfer bridge, where Mn_3O_4 behaves as a hole trapping cocatalyst (Potapenko et al., 2021; Xiang et al., 2019).

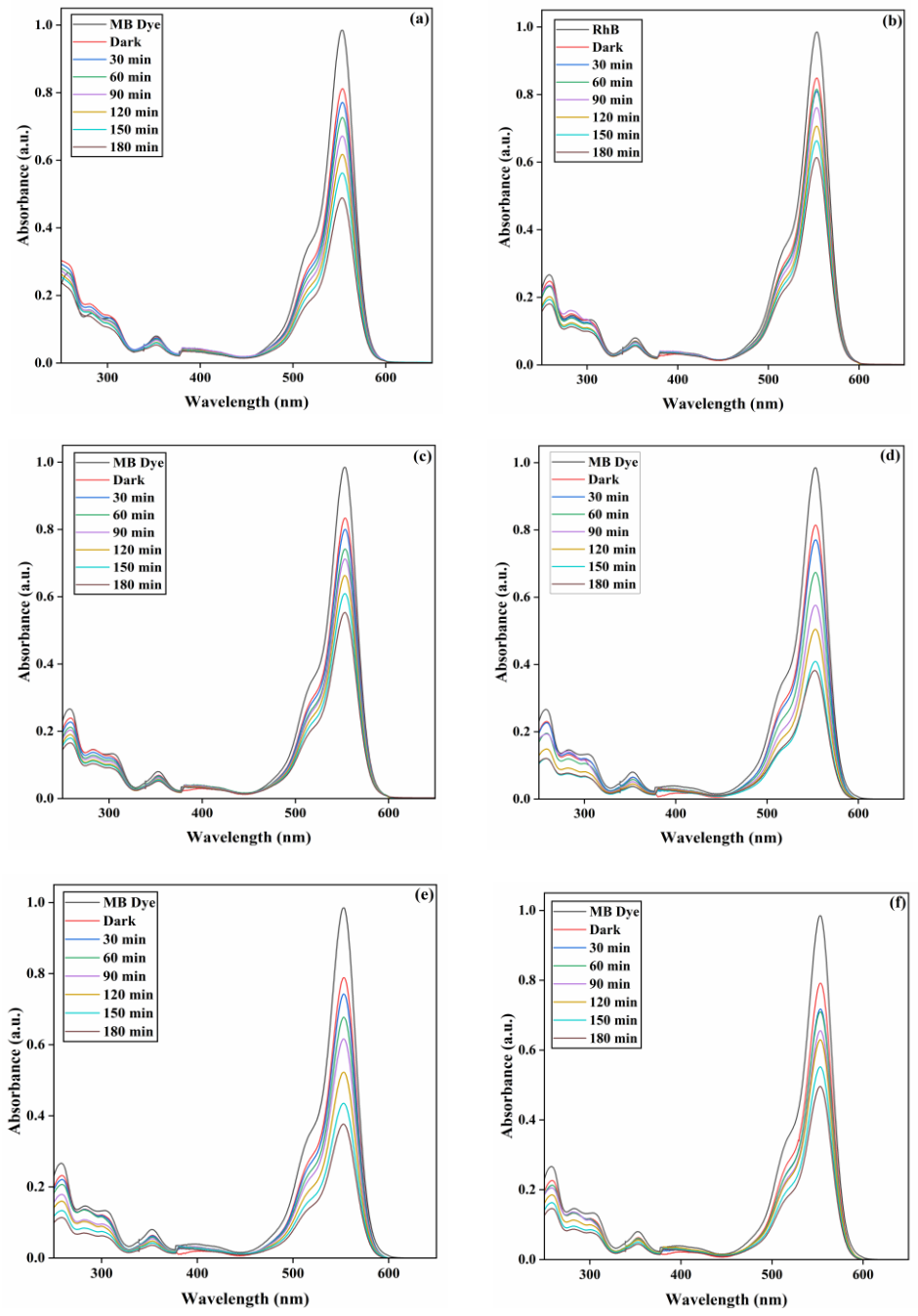

Figure 9. Time-dependent absorption spectra of pristine rhodamine B dye without UV irradiation in the absence of the photocatalyst and rhodamine-B dye for different intervals of UV irradiation in the presence of various photocatalysts (a) Mn_1Cu_0S NPs; (b) $Mn_{0.99}Cu_{0.01}S$ NPs; (c) $Mn_{0.97}Cu_{0.03}S$ NPs; (d) $Mn_{0.95}Cu_{0.05}S$ NPs; (e) $Mn_{0.93}Cu_{0.07}S$ NPs; (f) $Mn_{0.91}Cu_{0.09}S$ NPs.

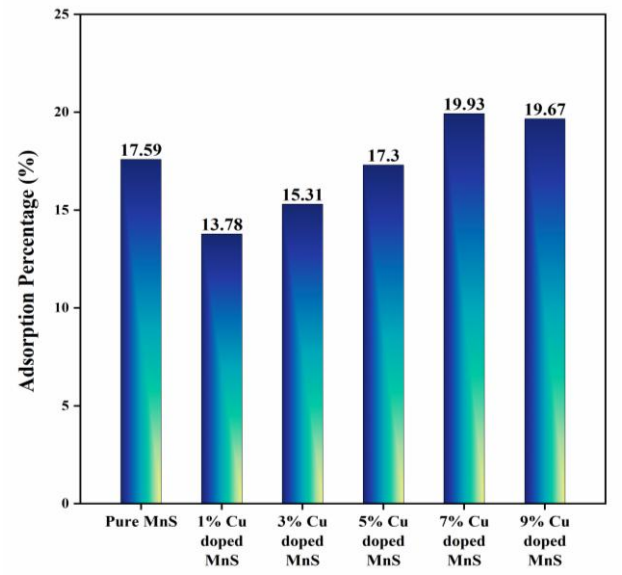

Figure 10. Dye adsorption percentage on the surface of synthesized $Mn_{1-x}Cu_xS$ ($0 \leq x \leq 0.09$) NPs after achieving adsorption-desorption equilibrium in the photocatalytic solution under dark conditions for 1 hour.

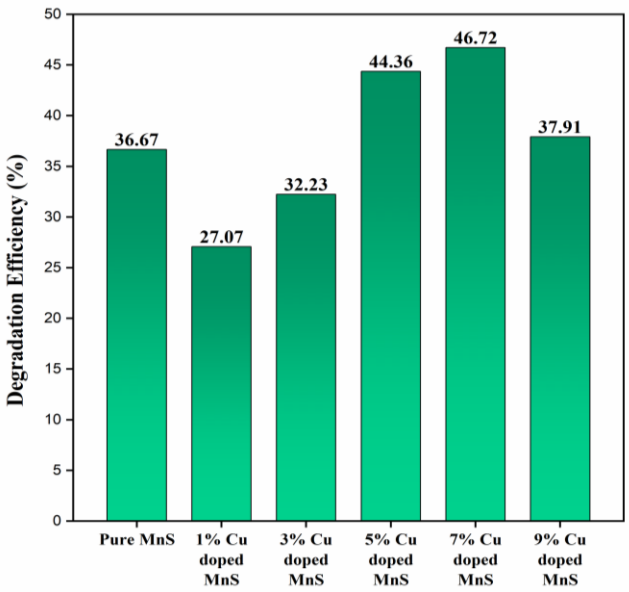

Figure 11. Photocatalytic degradation efficiency of $Mn_{1-x}Cu_xS$ ($0 \leq x \leq 0.09$) NPs.

4. Conclusions

The chemical co-precipitation is a facile and eco-friendly synthesis method, which gives a good yield of pristine MnS and Cu-doped MnS nanoparticles. Synthesized $Mn_{1-x}Cu_xS$ ($0 \leq x \leq 0.09$) nanoparticles crystallize in dual α-MnS phase and γ-MnS phase with average crystallite size values of 17.48 nm and 17.38 nm for Mn_1Cu_0S NPs and $Mn_{0.91}Cu_{0.09}S$ NPs, respectively. Copper doping in the MnS lattice prohibits the

particle growth due to compressive strain. Synthesized nanoparticles have cauliflower like morphology with average particle size values of 25 ± 8 nm and 21 ± 5 nm for Mn_1Cu_0S NPs and $Mn_{0.91}Cu_{0.09}S$ NPs, respectively. Spectroscopic studies reveal the direct UV band gap of synthesized nanoparticles, which broadens with doping due to strain. Synthesized nanoparticles show good photocatalytic activity potential towards the photo-degradation of RhB dye. Maximum degradation of RhB dye was attained for $Mn_{0.93}Cu_{0.07}S$ nanoparticles with a degradation efficiency of 46.72%. The photocatalytic activity dependence on doping concentration does not show a uniform trend due to the synergistic effect of the dual phase and lattice strain tunable particle morphology, absorption quantum yield, and bandgap. Nevertheless, these nanoparticles offer the potential to be a good photocatalyst for the degradation of organic pollutants, which can be explored in the future.

Conflicts of Interest

There are no conflicts of interest to declare.

Acknowledgments

The authors are grateful to the Sophisticated Analytical Instrumentation Facility (SAIF), Panjab University, Chandigarh, for providing FE-SEM, and EDX facilities. The authors sincerely acknowledge Thapar Institute of Engineering and Technology (TIET), Patiala, Punjab, for providing XRD facility. The authors gratefully acknowledge the financial support provided by Rashtriya Uchchatar Shiksha Abhiyan (RUSA-2) under component-10.

AI Disclosure

The author(s) declare that no assistance is taken from generative AI to write this article.

References

Admuthe, A., Kumbhar, S.S., Chougule, S.K., Padasare, G.N., & Tonape, M.M. (2020). Synthesis and characterization of MnS thin film at room temperature for supercapacitor application. *Macromolecular Symposia, 392*, 2000186. https://doi.org/10.1002/masy.202000186

Agoro, M.A., & Meyer, E.L. (2022). Proficient one-step heat-up synthesis of manganese sulfide quantum dots for solar cell applications. *Molecules*, *27*(19), 6678. https://doi.org/10.3390/molecules27196678

Ali, H., Shokr, E.K., Ismail, A., Kamel, M.S., Mohamed, H., & Hasaneen, M. (2024). Doping and precoating by Cu-metal and annealing impacts on some physical properties and applications of MnS thin films. *Optical Materials*, *148*, 114821. https://doi.org/https://doi.org/10.1016/j.optmat.2023.114821

Barry, R.G., & Chorley, R.J. (2009). *Atmosphere, weather and climate*. Routledge. New York. https://doi.org/10.4324/9780203871027

Brieler, F.J., Grundmann, P., Fröba, M., Chen, L., Klar, P.J., Heimbrodt, W., Krug von Nidda, H.-A., Kurz, T., & Loidl, A. (2004). Formation of $Zn_{1-x}Mn_xS$ nanowires within mesoporous silica of different pore sizes. *Journal of the American Chemical Society*, *126*(3), 797-807. https://doi.org/10.1021/ja038960j

Chen, T., Tang, Y., Qiao, Y., Liu, Z., Guo, W., Song, J., Mu, S., Yu, S., Zhao, Y., & Gao, F. (2016). All-solid-state high performance asymmetric supercapacitors based on novel MnS nanocrystal and activated carbon materials. *Scientific Reports*, *6*(1), 23289. https://doi.org/ 10.1038/srep23289

Chen, X., Shen, S., Guo, L., & Mao, S.S. (2010). Semiconductor-based photocatalytic hydrogen generation. *Chemical Reviews*, *110*(11), 6503-6570. https://doi.org/10.1021/cr1001645

Chen, Y., Jiang, D., Gong, Z., Li, Q., Shi, R., Yang, Z., Lei, Z., Li, J., & Wang, L.-N. (2020). Visible-light responsive organic nano-heterostructured photocatalysts for environmental remediation and H_2 generation. *Journal of Materials Science & Technology*, *38*, 93-106. https://doi.org/https://doi.org/10.1016/j.jmst.2019.09.003

Fan, D., Yang, X., Wang, H., Zhang, Y., & Yan, H. (2003). Photoluminescence of MnS thin film prepared by chemical bath deposition. *Physica B: Condensed Matter*, *337*(1-4), 165-169. https://doi.org/10.1016/S0921-4526(03)00399-5

Fujishima, A., & Honda, K. (1972). Electrochemical photolysis of water at a semiconductor electrode. *Nature*, *238*(5358), 37-38. https://doi.org/10.1038/238037a0

Gui, Y., Qian, L., & Qian, X. (2011). Hydrothermal synthesis of uniform rock salt (α-) MnS transformation from wurtzite (γ-) MnS. *Materials Chemistry and Physics*, *125*(3), 698-703. https://doi.org/10.1016/j.matchemphys.2010.09.071

Guo, Y., Zhou, X., Tang, J., Tanaka, S., Kaneti, Y.V., Na, J., Jiang, B., Yamauchi, Y., Bando, Y., & Sugahara, Y. (2020). Multiscale structural optimization: Highly efficient hollow iron-doped metal sulfide heterostructures as bifunctional electrocatalysts for water splitting. *Nano Energy*, *75*, 104913. https://doi.org/ 10.1016/j.nanoen.2020.104913

Hao, Y., Chen, C., Yang, X., Xiao, G., Zou, B., Yang, J., & Wang, C. (2017). Studies on intrinsic phase-dependent electrochemical properties of MnS nanocrystals as anodes for lithium-ion batteries. *Journal of Power Sources*, *338*, 9-16. https://doi.org/ 10.1016/j.jpowsour.2016.11.032

Heiba, Z.K., Mohamed, M.B., & Imam, N. (2015). Biphasic quantum dots of cubic and hexagonal Mn doped CdS; necessity of rietveld analysis. *Journal of Alloys and Compounds*, *618*, 280-286. https://doi.org/10.1016/j.jallcom.2014.08.106

Heiba, Z.K., Mohamed, M.B., Farag, N.M., & Badawi, A. (2022). Structural, optical and electronic characteristics of Cu and Mg-doped nano MnS sample prepared by molten salt solid state reaction. *Journal of Materials Science: Materials in Electronics*, *33*(13), 10388-10398. https://doi.org/10.1007/s10854-022-08026-x

Holzwarth, U., & Gibson, N. (2011). The Scherrer equation versus the 'Debye-Scherrer equation'. *Nature Nanotechnology*, *6*(9), 534-534. https://doi.org/10.1038/nnano.2011.145

Huffman, D.R., & Wild, R.L. (1967). Optical properties of α−MnS. *Physical Review*, *156*(3), 989. https://doi.org/10.1103/PhysRev.156.989

Ibrahim, S.G. (2021). Physical properties of chemically spray deposited nanocrystalline manganese sulfide (MnS) thin films. *Journal of Materials Science: Materials in Electronics*, *32*(1), 543-550. https://doi.org/10.1007/s10854-020-04837-y

Jamal, F., Rafique, A., Moeen, S., Haider, J., Nabgan, W., Haider, A., Imran, M., Nazir, G., Alhassan, M., & Ikram, M. (2023). Review of metal sulfide nanostructures and their applications. *ACS Applied Nano Materials*, *6*(9), 7077-7106. https://doi.org/10.1021/acsanm.3c00417

Janani, R., Rubashree, M., Kumar, B.H., Syed, A., Thomas, A.M., Bahkali, A.H., Elgorban, A.M., Raju, L.L., & Khan, S.S. (2020). Synthesis of CTAB functionalized MnS/PVP-Ag nanocomposite for Hg^{2+} detection, photocatalysis and antibacterial application. *Optical Materials*, *110*, 110452. https://doi.org/10.1016/j.optmat.2020.110452

Kayestha, R., & Hajela, K. (1995). ESR studies on the effect of ionic radii on displacement of Mn^{2+} bound to a soluble β-galactoside binding hepatic lectin. *FEBS Letters*, *368*(2), 285-288. https://doi.org/10.1016/0014-5793(95)00673-W

Kim, D.S., Lee, J.Y., Na, C.W., Yoon, S.W., Kim, S.Y., Park, J., Jo, Y., & Jung, M.-H. (2006). Synthesis and photoluminescence of Cd-doped α-MnS nanowires. *The Journal of Physical Chemistry B*, *110*(37), 18262-18266. https://doi.org/10.1021/jp063965z

Lalithambika, K., Shanmugapriya, K., & Sriram, S. (2019). Photocatalytic activity of MoS_2 nanoparticles: an experimental and DFT analysis. *Applied Physics A*, *125*(12), 817. https://doi.org/10.1007/s00339-019-3120-9

Lee, S., Song, M., Kim, S., Mathew, V., Sambandam, B., Hwang, J.-Y., & Kim, J. (2020). High lithium storage properties in a manganese sulfide anode via an intercalation-cum-conversion reaction. *Journal of Materials Chemistry A*, *8*(34), 17537-17549. https://doi.org/10.1039/D0TA05758D

Liu, D.H., Li, W.H., Zheng, Y.P., Cui, Z., Yan, X., Liu, D.S., Wang, J., Zhang, Y., Lü, H.Y., & Bai, F.Y. (2018). In situ encapsulating α-MnS into N, S-codoped nanotube-like carbon as advanced anode material: α→β phase transition promoted cycling stability and superior Li/Na-storage performance in Half/Full cells. *Advanced Materials*, *30*(21), 1706317. https://doi.org/10.1002/adma.201706317

Liu, J., Zheng, X., Shi, Z., & Zhang, S. (2014). Sulfur/mesoporous carbon composites combined with γ-MnS as cathode materials for lithium/sulfur batteries. *Ionics*, *20*(5), 659-664. https://doi.org/10.1007/s11581-013-1019-6

Liu, T., Li, Y., Yin, J., Li, J., & Wu, H. (2020). Hydrothermal synthesis of uniform urchin-like γ-MnS architectures and their photocatalytic properties. *Physica E: Low-dimensional Systems and Nanostructures*, *116*, 113711. https://doi.org/10.1016/j.physe.2019.113711

Lu, J., Qi, P., Peng, Y., Meng, Z., Yang, Z., Yu, W., & Qian, Y. (2001). Metastable MnS crystallites through solvothermal synthesis. *Chemistry of Materials*, *13*(6), 2169-2172. https://doi.org/10.1021/cm010049j

Ma, D., Huang, S., & Zhang, L. (2008). One-pot synthesis and magnetic, electrical properties of single-crystalline α-MnS nanobelts. *Chemical Physics Letters*, *462*(1-3), 96-99. https://doi.org/10.1016/j.cplett.2008.07.078

Makuła, P., Pacia, M., & Macyk, W. (2018). How to correctly determine the band gap energy of modified semiconductor photocatalysts based on UV–Vis spectra. *The Journal of Physical Chemistry Letters*, *9*(23), 6814-6817.

Michel, F., Schoonen, M., Zhang, X., Martin, S., & Parise, J. (2006). Hydrothermal synthesis of pure α-phase manganese (II) sulfide without the use of organic reagents. *Chemistry of Materials*, *18*(7), 1726-1736. https://doi.org/10.1021/cm048320v

Mills, A., & Le Hunte, S. (1997). An overview of semiconductor photocatalysis. *Journal of Photochemistry and Photobiology A: Chemistry*, *108*(1), 1-35. https://doi.org/10.1016/S1010-6030(97)00118-4

Mills, A., Davies, R.H., & Worsley, D. (1993). Water purification by semiconductor photocatalysis. *Chemical Society Reviews*, *22*(6), 417-425. https://doi.org/10.1039/CS9932200417

Muthu, S.S., Khadir, A., & Muthu (2021). *Novel materials for dye-containing wastewater treatment*. Springer. Singapore. https://doi.org/10.1007/978-981-16-2892-4

Pawar, R., & Lee, C.S. (2015). *Heterogeneous nanocomposite-photocatalysis for water purification*. William Andrew. New York. https://doi.org/10.1016.C2014-0-02650-0

Potapenko, K.O., Kurenkova, A.Y., Bukhtiyarov, A.V., Gerasimov, E.Y., Cherepanova, S.V., & Kozlova, E.A. (2021). Comparative study of the photocatalytic hydrogen evolution over $Cd_{1-x}Mn_xS$ and CdS-β-Mn_3O_4-MnOOH photocatalysts under visible light. *Nanomaterials*, *11*(2), 355. https://doi.org/10.3390/nano11020355

Puglisi, A., Mondini, S., Cenedese, S., Ferretti, A.M., Santo, N., & Ponti, A. (2010). Monodisperse octahedral α-MnS and MnO nanoparticles by the decomposition of manganese oleate in the presence of sulfur. *Chemistry of Materials*, *22*(9), 2804-2813. https://doi.org/10.1021/cm903735e

Qurashi, A. (2014). *Metal chalcogenide nanostructures for renewable energy applications*. John Wiley & Sons. New Jersey. https://doi.org/10.1002/9781119008934

Rao, C., & Pisharody, K. (1976). Transition metal sulfides. *Progress in Solid State Chemistry*, *10*, 207-270. https://doi.org/10.1016/0079-6786(76)90009-1

Rui, X., Tan, H., & Yan, Q. (2014). Nanostructured metal sulfides for energy storage. *Nanoscale*, *6*(17), 9889-9924. https://doi.org/10.1039/C4NR03057E

Salem, M.A., Khan, A.M., & Manea, Y.K. (2022). A novel nano-hybrid carbon architecture as chemo sensor for natural hazards: active adsorption of Rose Bengal dye and detection of hazard pollutants at ppb level. *Journal of Environmental Chemical Engineering*, *10*(1), 107032. https://doi.org/10.1016/j.jece.2021.107032

Shanker, U., Rani, M., & Jassal, V. (2017). Degradation of hazardous organic dyes in water by nanomaterials. *Environmental Chemistry Letters*, *15*(4), 623-642. https://doi.org/10.1007/s10311-017-0650-2

Somnath, Ahmad, M., & Siddiqui, K.A. (2022). Synthesis of a mixed-ligand H-bonded Cu coordination polymer: exploring the pH-dependent high photocatalytic degradation of rhodamine 6G, methyl violet, crystal violet, and rose Bengal dyes under room illumination. *ACS Omega*, *7*(45), 41120-41136. https://doi.org/10.1021/acsomega.2c04669

Swathi, S., Yuvakkumar, R., Kumar, P.S., Ravi, G., & Velauthapillai, D. (2021). Hydrothermally synthesized α-MnS nanostructures for electrochemical water oxidation and photocatalytic hydrogen production. *Fuel*, *303*, 121293. https://doi.org/10.1016/j.fuel.2021.121293

Thompson, A.C., & Vaughan, D. (2001). *X-ray data booklet* (Vol. 8). Lawrence Berkeley National Laboratory, University of California Berkeley, CA. https://doi.org/10.2172/6359890

Uma, P.I., Shenoy, U.S., & Bhat, D.K. (2023). Doped BaTiO3 cuboctahedral nanoparticles: role of copper in photocatalytic degradation of dyes. *Applied Surface Science Advances*, *15*, 100408. https://doi.org/10.1016/j.apsadv.2023.100408

Veeramanikandasamy, T., Rajendran, K., Sambath, K., & Rameshbabu, P. (2016). Effect of Cu-doping on optical, electrical and magnetic properties of chemically synthesized MnS nanocrystals. *Materials Chemistry and Physics*, *171*, 328-335. https://doi.org/10.1016/j.matchemphys.2016.01.024

Viswanath, R., Naik, H.B., Kumar, G.Y., Kumar, P.P., Harish, K., & Prabhakara, M. (2014). Luminescence properties of blue–red emitting multilayer coated single structure ZnS/MnS/ZnS nanocomposites. *Spectrochimica Acta Part A: Molecular and Biomolecular Spectroscopy*, *125*, 222-227. https://doi.org/10.1016/j.saa.2014.01.022

Wang, H., Yang, Y., Liu, J., Wu, H., Wu, K., Lyu, C., Wu, J., Lau, W.-M., Wu, Q., & Zheng, J. (2023). The role of manganese-based catalyst in electrocatalytic water splitting: recent research and progress. *Materials Today Physics*, *36*, 101169. https://doi.org/10.1016/j.mtphys.2023.101169

Wang, L., Sivananthan, S., Sporken, R., & Caudano, R. (1996). Interface properties and valence-band discontinuity of MnS/ZnSe heterostructures. *Physical Review B*, *54*(4), 2718. https://doi.org/10.1103/PhysRevB.54.2718

Woetzel, J., Pinner, D., Samandari, H., Engel, H., Krishnan, M., Boland, B., & Powis, C. (2020). *Climate risk and response*.https://www.mckinsey.com/~/media/mckinsey/business%20functions/sustainability/our%20insights/climate%20risk%20and%20response%20physical%20hazards%20and%20socioeconomic%20impacts/mgi-climate-risk-and-response-full-report-vf.pdf

Xiang, J., Dan, M., Cai, Q., Yu, S., & Zhou, Y. (2019). Graphene oxide induced dual cocatalysts formation on manganese sulfide with enhanced photocatalytic hydrogen production from hydrogen sulfide. *Applied Surface Science*, *494*, 700-707. https://doi.org/10.1016/j.apsusc.2019.07.219

Yang, X., Wang, Y., Wang, K., Sui, Y., Zhang, M., Li, B., Ma, Y., Liu, B., Zou, G., & Zou, B. (2012). Polymorphism and formation mechanism of nanobipods in manganese sulfide nanocrystals induced by temperature or pressure. *The Journal of Physical Chemistry C*, *116*(5), 3292-3297. https://doi.org/10.1021/jp209591r

Yıldırım, M.A., Yıldırım, S.T., Cavanmirza, İ., & Ateş, A. (2016). Chemically synthesis and characterization of MnS thin films by SILAR method. *Chemical Physics Letters*, *647*, 73-78. https://doi.org/10.1016/j.cplett.2016.01.048